Available online at www.sciencedirect.com
ScienceDirect
Materials Science and Engineering C 28 (2008) 406–413
MATERIALS SCIENCE & ENGINEERING C
www.elsevier.com/locate/msec

In situ X-ray analysis of mechanism of nonlinear super elastic behavior of Ti–Nb–Ta–Zr system beta-type titanium alloy for biomedical applications

Mitsuo Niinomi *, Toshikazu Akahori, Masaaki Nakai

Department of Biomaterials Science, Institute for Materials Research, Tohoku University, 2-1-1, Katahira, Aoba-ku, Sendai 980-8577, Japan

Available online 14 April 2007

Abstract

Ti–XNb–10Ta–5Zr (mass %) alloys based on nominal compositions of Ti–35Nb–10Ta–5Zr, Ti–30Nb–10Ta–5Zr, and Ti–25Nb–10Ta–5Zr were fabricated through powder metallurgy and forging and swaging processes for biomedical applications. The tensile deformation mechanisms of the Ti–25Nb–10Ta–5Zr, Ti–30Nb–10Ta–5Zr, and Ti–35Nb–10Ta–5Zr alloys were investigated *in situ* by X-ray diffraction analysis under several loading conditions.

Under the loading conditions, the X-ray diffraction peaks of all the specimens shifted to higher angles than those obtained under the unloading conditions. For the Ti–30Nb–10Ta–5Zr alloy, the elastic deformation is considered to progress continuously in a different crystal direction although after the elastic strain reaches elastic limit in the crystal direction where the elastic limit is the smallest, slip deformation occurs in that crystal direction. The elastic modulus of this alloy appears to decrease in terms of strain over the proportional limit. Thus, the elastic deformation behavior of the Ti–30Nb–10Ta–5Zr alloy does not obey Hooke's law.

Keywords: Beta type titanium alloy; Elastic plastic deformation; Super elasticity; X-ray analysis; Biomaterial

1. Introduction

Ti–Nb–Ta–Zr system alloys such as Ti–29 mass%Nb–13 mass%Ta–4.6 mass%Zr [1–6] (mass% in chemical compositions of the alloys will be omitted hereafter) and Ti–35Nb–7Zr–5Ta are expected to be used as biomaterials because they exhibit excellent biocompatibility and very low Young's moduli [7]. The authors investigated the effects of alloying elements on the mechanical properties and tensile deformation behavior of Ti–XNb–10Ta–5Zr, Ti–30Nb–XTa–5Zr and Ti–30Nb–10Ta–XZr, which are alloys wherein each alloying element of Ti–30Nb–10Ta–5Zr – whose chemical composition is the simplified chemical composition of Ti–29Nb–13Ta–4.6Zr – was systematically changed [8,9]. Further, they have reported [10–12] that the elastic deformation behavior of Ti–30Nb–10Ta–5Zr does not obey Hooke's law. However, the detailed mechanisms of the elastic deformation behavior of the Ti–30Nb–10Ta–5Zr alloy are not yet clearly understood.

In this study, Ti–30Nb–10Ta–5Zr, Ti–25Nb–10Ta–5Zr, and Ti–35Nb–10Ta–5Zr alloys were fabricated by powder metallurgy and forging processes. The changes in the constituent phases and X-ray diffraction profiles of these alloys were investigated by X-ray diffraction analysis under tensile loading and unloading conditions. Finally, the mechanisms of the elastic behavior of these alloys were discussed in this study.

2. Experimental procedures

2.1. Materials

The materials used in this study were Ti–25Nb–10Ta–5Zr, Ti–30Nb–10Ta–5Zr, and Ti–35Nb–10Ta–5Zr (hereafter referred to as $TNTZ_{25}$, $TNTZ_{30}$, and $TNTZ_{35}$, respectively) that are beta-type titanium alloys fabricated through powder metallurgy and forging and swaging processes, which will be mentioned below. A beta-type titanium alloy, Ti–15V–3Cr–3Sn–3Al (hereafter referred to as Ti_{15-3}), a ferrite carbon steel, S45C (hereafter, referred to as S45C), with a large amount of the bcc phase similar to beta-type titanium alloys, and the A1070

* Corresponding author.
E-mail address: niinomi@imr.tohoku.ac.jp (M. Niinomi).

0928-4931/$ - see front matter © 2007 Elsevier B.V. All rights reserved.
doi:10.1016/j.msec.2007.04.028

aluminum alloy (hereafter referred to as A1070) with a fcc crystal structure that is different from beta-type titanium alloys were also used for comparison. The Ti_{15-3}, S45C, and A1070 are commercially available alloys.

The blended elemental powder metallurgy process was applied to fabricate the main materials $TNTZ_{25}$, $TNTZ_{30}$, and $TNTZ_{35}$. The mean particle diameters and purity of the powdered alloying elements used in this study were below 45 μm and above 99.8%, respectively (Ti powder: Sitix of Amagasaki, Inc., Japan; Nb powder: H. C. Starck GmbH and Co. KG., Germany; Ta powder: H. C. Stack–VTECH Ltd., Japan; and Zr powder: Kojundo Chemical Lab. Co., Ltd., Japan). The powders of the alloying elements were mixed to achieve each target chemical composition and then pressed by a cold isostatic pressing machine to form a green product with a diameter of 40 mm and a length of approximately 100 mm. Each green product was then sintered at 1573 K for 57.3 ks in a vacuum of approximately 1.33×10^{-3} Pa. Subsequently, each sintered green product was forged and swaged at 1223 K to form a bar with a diameter of 10 mm. Finally each swaged bar was subjected to heat treatment at 1123 K for 1.8 ks followed by air cooling [8] in order to remove the residual stress from the hot forging and swaging. The chemical compositions of each alloy are listed in Table 1.

Ti_{15-3} alloy was subjected to solution treatment at 1103 K for 3.6 ks in vacuum followed by water quenching. The S45C alloy was subjected to a full annealing treatment at 1083 K for 3.6 ks in vacuum followed by furnace cooling. The A1070 alloy was subjected to an annealing treatment at 623 K for 3.6 ks in vacuum followed by furnace cooling.

The plate tensile specimens shown in Fig. 1 were fabricated from the treated material by electric discharge method.

2.2. Tensile tests and X-ray diffraction analysis under tensile loading conditions

The tensile specimens were wet-polished using waterproof emery papers up to #1500 and then subjected to X-ray diffraction analysis under various tensile unloading and loading conditions. A photograph of the X-ray diffractometer with a tensile specimen fixture-jig is shown in Fig. 2. The tensile specimen was fixed to the jig attached to the X-ray diffractometer shown in Fig. 2 and was deformed to a specific strain as will be mentioned subsequently by manual operation. The jig fixed with the deformed specimen was placed into the chamber of the X-ray diffractometer and then subjected to X-ray diffraction analysis (XRD). In XRD, the accelerating voltage, current and scanning angle (2θ) were 40 kV, 30 mA, and 65°–85°, respectively. The deformation degree was adjusted for the strain to be 0% (unloading conditions),

Table 1
Chemical compositions of the Ti–XNb–10Ta–5Zr (mass%) alloys

	$TNTZ_{25}$	$TNTZ_{30}$	$TNTZ_{35}$
Ti	bal.	bal.	bal.
Nb	24.9	29.4	35.0
Ta	9.94	10.4	9.96
Zr	4.62	4.80	4.53
O	0.23	0.23	0.24

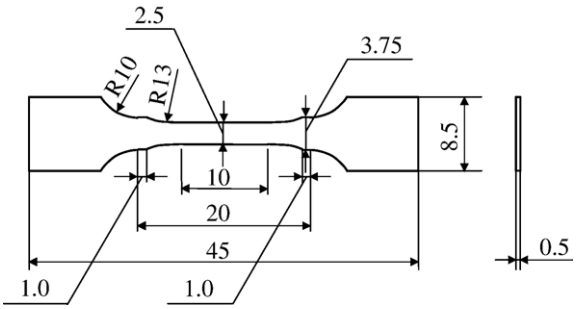

Fig. 1. Schematic drawing of specimen. All units are in mm.

approximately 1.5%, and approximately 10% by measuring the strain using a foil strain gage attached directly to the gage section of the specimen and also by measuring a change in the gage length using a reading microscope.

General tensile tests were carried out on specimens with the same geometry and finish conditions using an Instron-type machine with a cross head speed of 8.33×10^{-6} m/s in air at room temperature. The load and strain were measured using the load cell of the machine and the foil strain gage attached to the gage section of the specimen, respectively.

2.3. Microstructural observations and in situ observation of specimen surface using a scanning electron microscope (SEM)

Each tensile specimen was mirror-finished by buff polishing using Al_2O_3 with a diameter of 0.06 μm after being polishing with a #1500 waterproof emery paper. After mirror-finishing, each specimen was tensile-tested using an electro-hydraulic machine with a capacity of 5 kN, while *in situ* observations of the specimen surface were simultaneously performed using an SEM attached to the electro-hydraulic machine. The SEM images or photographs will be shown by inverting the black and white contrast in order to emphasize the unevenness in the SEM images in this study.

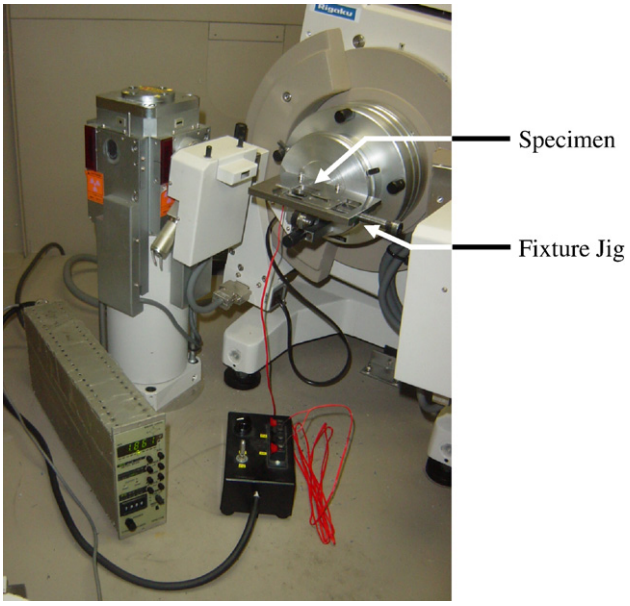

Fig. 2. Photograph of X-ray diffract meter with fixture-jig for specimen.

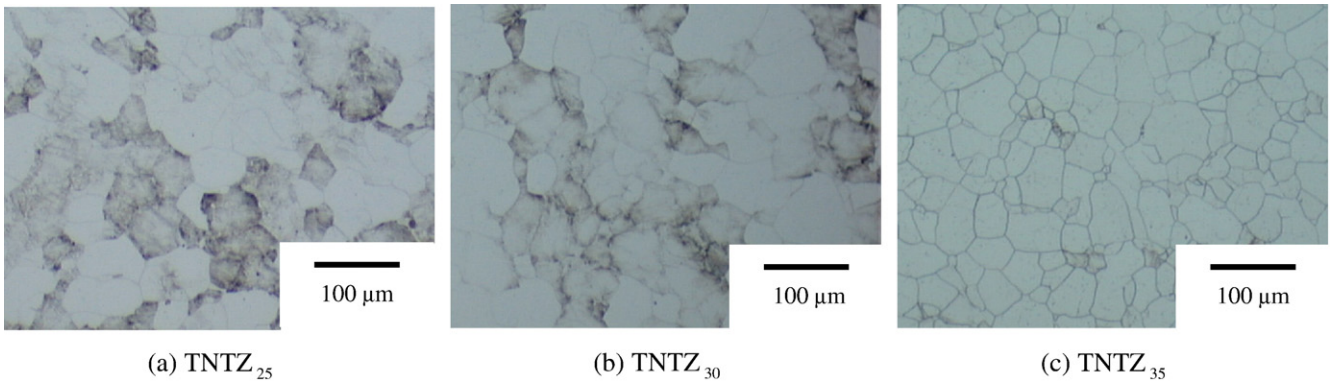

Fig. 3. Optical micrographs of Ti–XNb–10Ta–5Zr: (a) $TNTZ_{25}$, (b) $TNTZ_{30}$ and (c) $TNTZ_{35}$ alloys.

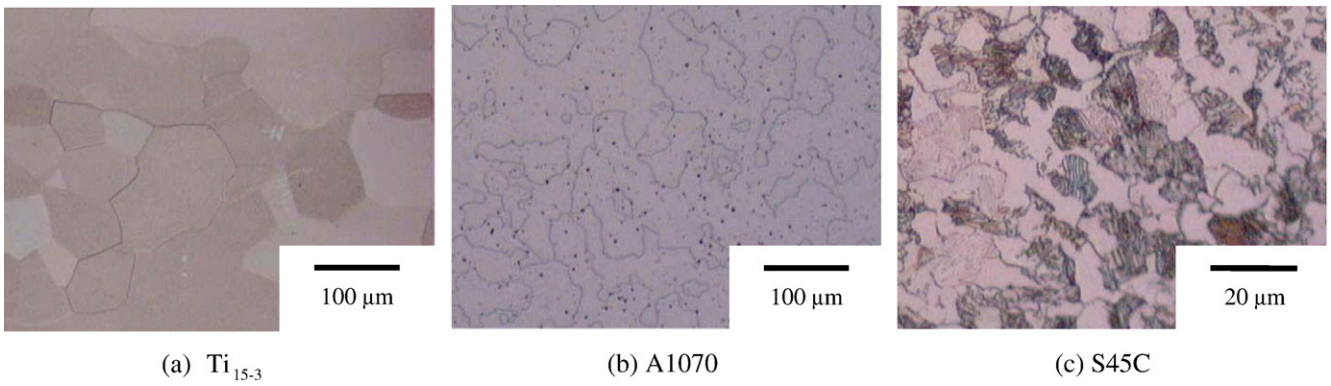

Fig. 4. Optical micrographs of (a) Ti_{15-3}, (b) A1070 and (c) S45C alloys.

Each specimen was etched in a 5% HF solution. The S45C specimen was etched in 1% nital. Each etched specimen was subjected to microstructural observation using an optical microscope.

3. Results and discussion

3.1. Microstructure

Fig. 3 shows the optical micrographs of $TNTZ_{25}$, $TNTZ_{30}$, and $TNTZ_{35}$ alloy. The micrograph of each TNTZ alloy shows equiaxed β grains. The mean diameters of $TNTZ_{25}$, $TNTZ_{30}$, and $TNTZ_{35}$ alloys were 56 μm, 62 μm, and 63 μm, respectively.

Fig. 4 shows the optical micrographs of Ti_{15-3}, A1070, and S45C alloy. The micrograph of Ti_{15-3} alloy shows equiaxed grains with a mean diameter of 118 μm. The micrograph of A1070 alloy shows a fairy large number of pits, which are formed due to the preferential dissolution of aluminum-iron intermetallic compounds (for example, $FeAl_3$) [13]. The micrograph of S45C shows the ferrite and pearlite phases.

3.2. Stress–strain curve

Fig. 5 shows the stress–strain curves obtained from tensile testing the $TNTZ_{25}$, $TNTZ_{30}$, and $TNTZ_{35}$ alloys. Fig. 6 shows the enlarged low strain regions (strain ε = 0%–2.0%) of the stress–strain curves of the $TNTZ_{25}$, $TNTZ_{30}$, and $TNTZ_{35}$ alloys. The shapes of the stress–strain curves of the Ti–XNb–10Ta–5Zr alloy change drastically with the content of Nb. It has been reported that the plastic deformation of the $TNTZ_{25}$ alloy is mainly due to the deformation-induced martensite transformation from the β phase to the α″ martensite phase, while the plastic deformation of the $TNTZ_{30}$ and $TNTZ_{35}$ alloys is mainly due to the slip [9, 10, 11].

The yielding phenomenon is clearly observed in the stress–strain curves of the $TNTZ_{25}$ and $TNTZ_{35}$ alloys. As compared to

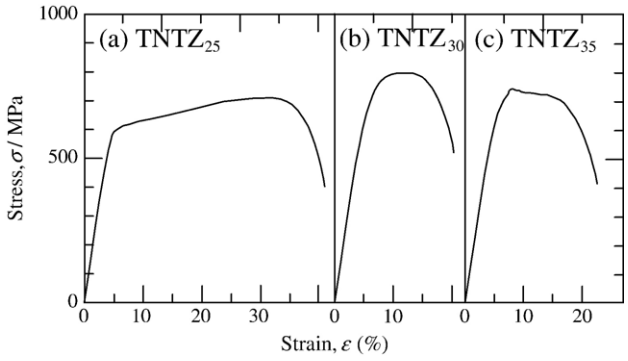

Fig. 5. Tensile stress–strain curves of Ti–XNb–10Ta–5Zr: (a) $TNTZ_{25}$, (b) $TNTZ_{30}$ and (c) $TNTZ_{35}$ alloys.

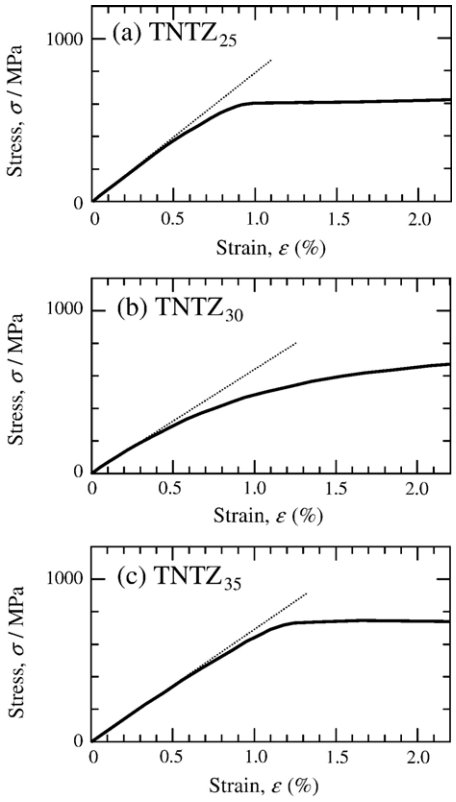

Fig. 6. Tensile stress–strain curves of Ti–XNb–10Ta–5Zr in low strain areas: (a) $TNTZ_{25}$, (b) $TNTZ_{30}$ and (c) $TNTZ_{35}$ alloys.

the $TNTZ_{25}$ and $TNTZ_{35}$ alloys, the stress–strain curve of the $TNTZ_{30}$ alloy does not show a clear yielding phenomenon. The stress of $TNTZ_{30}$ alloy does not increase linearly with an increase in strain even during the first loading. The elastic deformation of $TNTZ_{30}$ alloy portrays the elastic-plastic behavior and disobeys Hooke's law.

3.3. Change in specimen surface morphology with tensile deformation

Fig. 7 shows the SEM micrographs of the surface of the $TNTZ_{25}$ alloy under various loading conditions obtained by *in situ* observations of the specimen surface. Linear irregularities appear on the surface of the specimen with increasing stress. These irregularities are considered to be the traces of the deformation-induced α″ phase or deformation twins. It has already been reported that the deformation twins are formed in addition to the deformation-induced α″ phase due to tensile loading [8].

Fig. 8 shows the SEM micrographs of the surface of the $TNTZ_{30}$ alloy under the various loading conditions obtained by *in situ* observations of the specimen surface. Curved irregularities can be clearly observed at the grain boundary at a stress of 726 MPa (Fig. 8 (a)). Linear irregularities, which are considered to be slip lines, appeared in the grains at a stress of 772 MPa (Fig. 8 (c)).

Fig. 9 also shows the SEM micrograph of the surface of $TNTZ_{35}$ at a stress of 710 MPa obtained by *in situ* observations of the specimen surface. Curved irregularities at the grain boundary and linear irregularities in the grains, which are considered to be slip lines, are observed similar to the case of $TNTZ_{30}$ alloy. However, these irregularities appeared simultaneously.

3.4. X-ray diffraction profiles under tensile loading conditions

Fig. 10 shows the *in situ* XRD profiles of the $TNTZ_{30}$ alloy under various loading conditions. Only a β phase peak is observed on the diffraction profiles of the $TNTZ_{30}$ alloy at 0%, 1.5%, 3.2%, and 9.4% strains under the unloading condition for each strain. The deformation-induced transformation from the β phase to the α″ martensite phase might not occur in the $TNTZ_{30}$ alloy. Therefore, the mechanism of the nonlinear elastic deformation is considered not to be due to the deformation-induced α″ martensite transformation but due to another mechanism. The peaks of the β phase shift to the high angle side under the loading conditions as compared with those under unloading conditions. This shift is considered to be due to the distortion of the lattice.

Fig. 11 shows the *in situ* XRD profiles of the $TNTZ_{25}$ alloy under various loading conditions. Only β phase peaks are observed in the XRD profiles obtained under the non-loading and unloading conditions at a strain of 1.6% while, α″ phase peaks are observed in those obtained under the loading and unloading conditions at strains of 3.1% and 9.8%. The deformation-induced α″ transformation in this study is similar

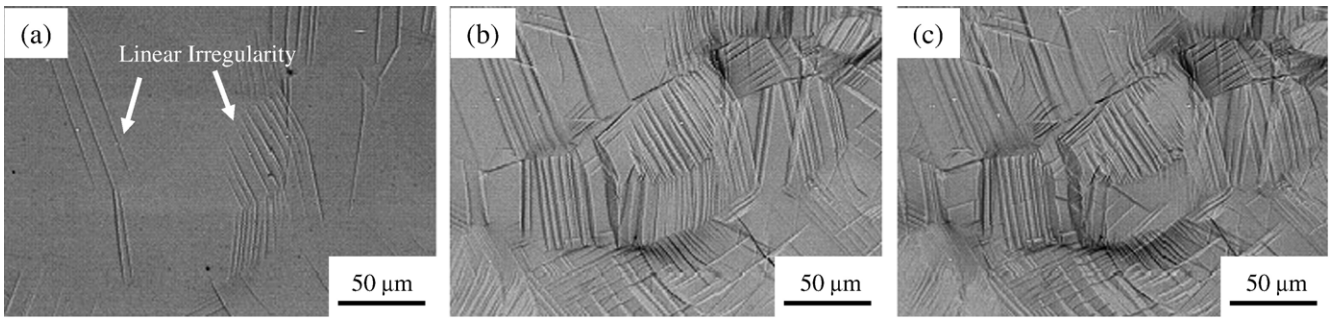

Fig. 7. SEM micrographs on surfaces of $TNTZ_{25}$ alloy under various loading conditions where loading stresses are (a) 599 MPa, (b) 623 MPa and (c) 638 MPa.

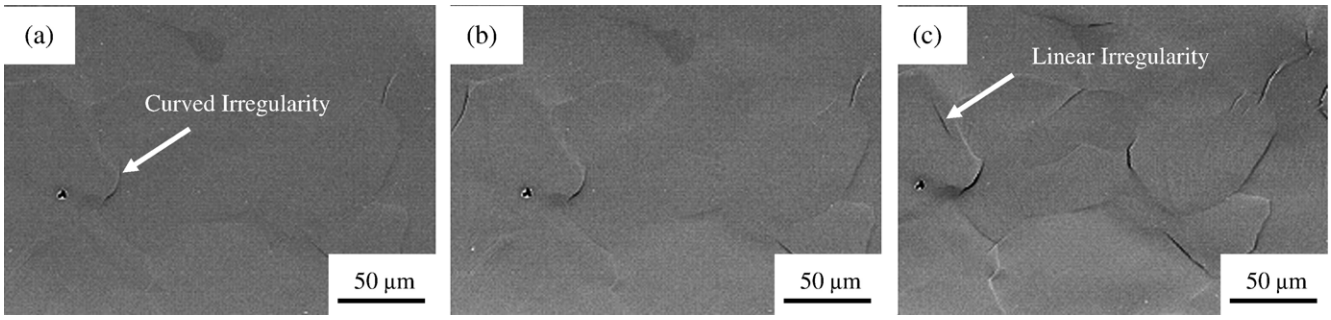

Fig. 8. SEM micrographs on surfaces of $TNTZ_{30}$ alloy under various loading conditions where loading stresses are (a) 726 MPa, (b) 749 MPa and (c) 772 MPa.

to that reported elsewhere [8-11]. The peaks of the β phase shift to the high angle side similar to the case of the $TNTZ_{30}$ alloy.

Fig. 12 shows the *in situ* XRD profiles of the $TNTZ_{35}$ alloy under the various loading conditions. Only β phase peaks are observed in every case, and they shift to the high angle side similar to the case of the $TNTZ_{30}$ alloy.

Fig. 13 shows the relationships between the tensile strain (ε) and lattice strain (ε_l) that is calculated from the X-ray diffraction peaks using the following equation for the $TNTZ_{25}$, $TNTZ_{30}$, $TNTZ_{35}$, $Ti_{15\text{-}3}$, A1070, and S45C alloys by assuming that the shrinking direction of the lattice is positive.

$$\varepsilon_l = \{(a_0 - a)/a_0\} \times 100 \quad (1)$$

where a_0 and a are the lattice constant under the no-load conditions and that under the tensile loading conditions, respectively.

The ε_l values of the $TNTZ_{25}$, $TNTZ_{30}$, and $TNTZ_{35}$ alloys were calculated using the diffraction angle of (211) of the β phase. The ε_l values of the S45C and A1070 alloys were calculated using the diffraction angle of (200) of the ferrite phase and that of (220), respectively.

In this study, the lattice was calculated to be shrinking due to the tensile loading because the tensile axis crosses the rotating axis of the specimen at right angles; therefore, XRD only from the crystal plane that shrinks due to Poisson's ratio occurred.

Fig. 14 shows the strains at the proportional limits obtained from the stress–strain curves of the $TNTZ_{25}$, $TNTZ_{30}$, $TNTZ_{35}$, A1070, and S45C alloys. The greater the strain at the proportional limits of the material, the greater is ε_l shown in Fig. 13. The large magnitude of the ε_l under the tensile loading conditions can be considered to depend on the maximum permissible elastic strain for the lattice; this strain will be hereafter referred to as the maximum lattice strain (ε_{emax}).

3.5. Mechanism of elastic deformation of $TNTZ_{30}$ and $TNTZ_{35}$ alloys

Fig. 15 shows the relationships between the tensile strain (ε) and lattice strain (ε_l) calculated at several diffraction angles of the $TNTZ_{30}$, and S45C alloys. The lattice strains of the $TNTZ_{30}$ and S45C alloys were calculated using the diffraction angles of (110), (200) and (211) for the β or the ferrite phase.

For the $TNTZ_{30}$ alloy, the value of the ε_l is remarkably different according to the diffraction angle used for the calculation. The ε_l values increase rapidly up to ε=3.0% and increase gradually above ε=3.0%. An increase in ε_l is attributed to the distortion of the lattice caused by the dislocations etc. introduced in the crystals. Since each value of ε_l is remarkably different in the low strain region up to ε=1.5%, the value of ε_{emax} is different according to the crystal orientation of the $TNTZ_{30}$ alloy. This trend was also recognized in the $TNTZ_{25}$ and $TNTZ_{35}$ alloys.

It has been reported that the Young's moduli of pure metals with the bcc structure, such as Li, Ba, Na, K, Rb, Fe, Ta, W, Cr, Mo, V and Nb are different according to the crystal direction [14]. Young's modulus of polycrystalline Ta, for example, is

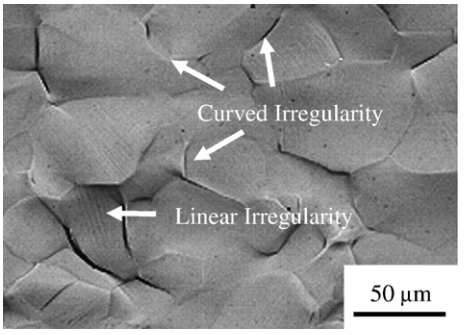

Fig. 9. SEM micrograph of $TNTZ_{35}$ alloy at a stress of 710 MPa.

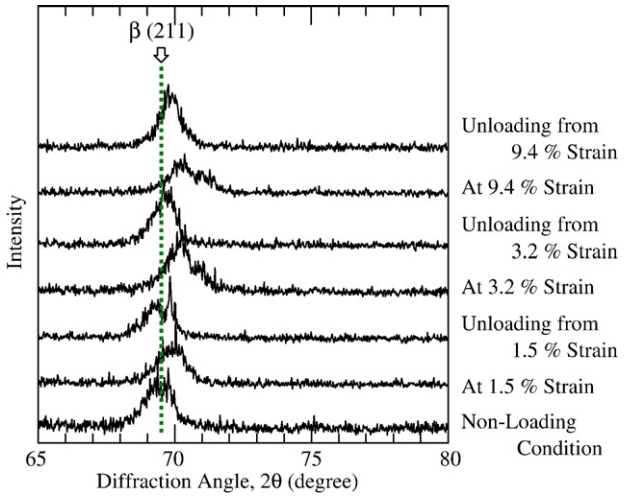

Fig. 10. XRD profiles of $TNTZ_{30}$ alloy at various loading conditions.

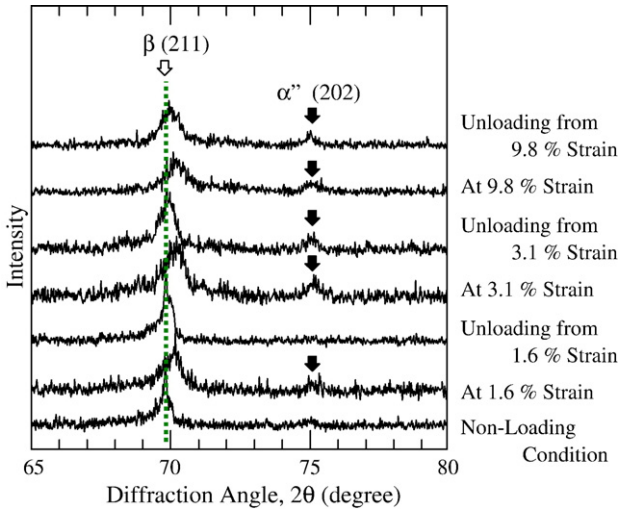

Fig. 11. X-ray diffraction profiles of $TNTZ_{25}$ alloy at various loading conditions.

181 GPa, but that of <100> is 146 GPa. Therefore, for β type titanium alloys with the bcc structure, the Young's modulus should be also different according to the crystal direction; ε_{emax} then displays anisotropy.

The microstructure of the S45C alloy comprises the ferrite and pearlite phases, and the ferrite phase is predominant in the entire microstructure. The crystal structure of ferrite is bcc and is similar to that of β titanium alloys. However, a change in the value of ε_l is much smaller as compared with the case of the $TNTZ_{30}$ alloy although it changes according to the diffraction angle used for the calculation. For the 1070 alloy with the fcc structure, the values of ε_l calculated using the diffraction angles of (111), (200), (220), and (311) were hardly different from each other and their trend in the change was similar to that in the case of the S45C alloy. Therefore, the remarkable anisotropy of ε_{emax} for β type titanium alloys is considered to have an intrinsic nature. However, further investigations are needed on this point.

For β type titanium alloys, the mechanism of plastic deformation changes in the order of α″ transformation twinning

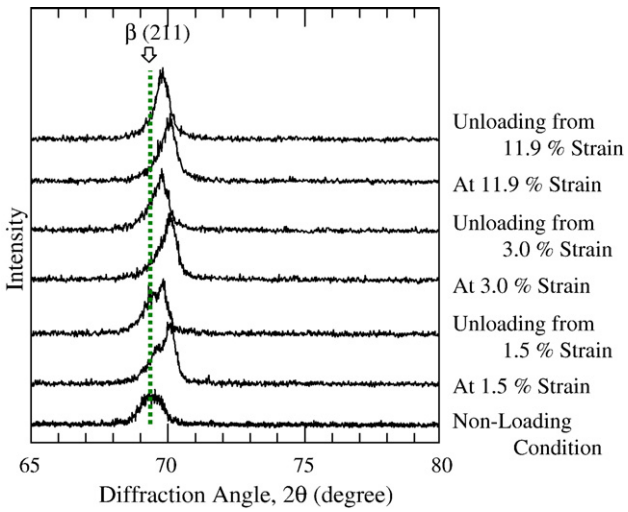

Fig. 12. X-ray diffraction profiles of $TNTZ_{35}$ alloy at various loading conditions.

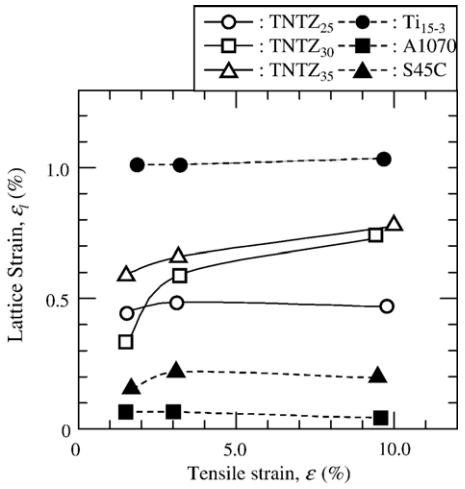

Fig. 13. Relationships between tensile strain and lattice strain of Ti–XNb–10Ta–5Zr, Ti_{15-3}, A1070 and S45C alloys.

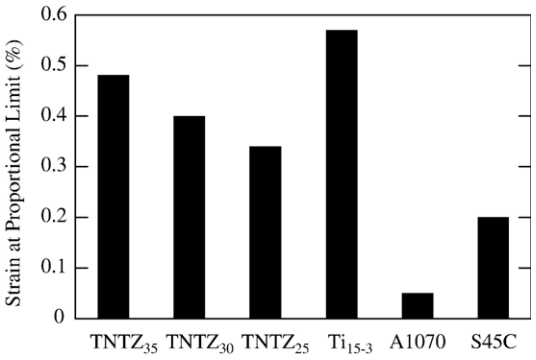

Fig. 14. Strain at proportional limits obtained from stress–strain curves of Ti–XNb–10Ta–5Zr, Ti_{15-3}, A1070 and S45C alloys.

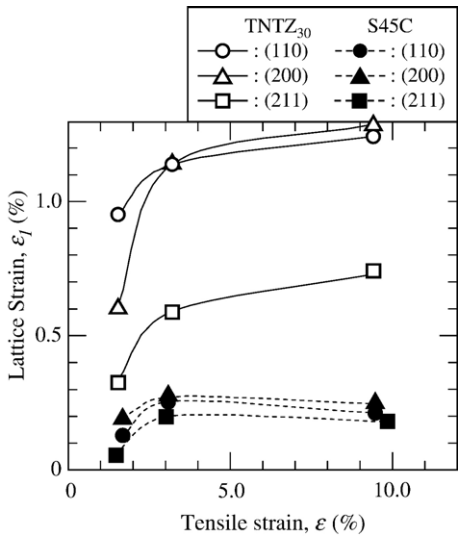

Fig. 15. Relationships between tensile strain and lattice strain calculated using several diffraction angles of $TNTZ_{30}$ and S45C alloys.

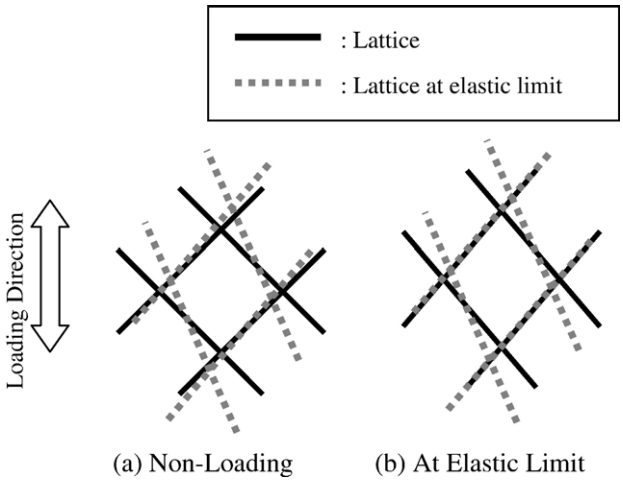

Fig. 16. Schematic drawings of deformation behavior of lattice in $TNTZ_{35}$ alloy.

and slip with an increase in the amount of β stabilizing elements [15, 16]. Therefore, it can be considered that the higher the amount of the stabilizing elements in an alloy, the higher is the dislocation activity.

Fig. 16 shows a schematic drawing of the deformation behavior of the lattice of the $TNTZ_{35}$ alloy. Since the lattice is distorted due to deformation, ε_l increases with ε in the elastic deformation region: this is understood from the results of XRD profiles obtained under the tensile loading conditions, as shown in Fig. 12. ε_{emax} shows anisotropy according to the crystal orientation in $TNTZ_{35}$ alloy as stated above. As ε increases, after ε_l reaches ε_{emax} in the crystal direction where ε_{emax} is the smallest as shown in Fig. 16 (b), slip deformation occurs in that crystal direction. The amount of the strain of the specimen at the instant ε_l reaches ε_{emax} in the crystal direction where ε_{emax} is the smallest is considered to be equivalent to that at the proportional limit shown in Fig. 14.

Fig. 17 shows a schematic drawing of the deformation behavior of the lattice of the $TNTZ_{30}$ alloy. This lattice is also distorted due to deformation similar to the case of the $TNTZ_{35}$ alloy. However, since the generation of the dislocations is considered to be difficult, the elastic deformation progresses continuously with the plastic deformation in the low strain region near the proportional limit. For the $TNTZ_{35}$ alloy, the ratio of the elastic deformation to plastic deformation is considered to be very small although the elastic deformation also progresses with the plastic deformation. For the $TNTZ_{30}$ alloy, the elastic deformation is considered to progresses continuously in a different crystal direction although after ε_l reaches ε_{emax} in the crystal direction where ε_{emax} is the smallest (Fig. 17 (b)), slip deformation occurs in that crystal direction. Since the plastic deformation occurs, and simultaneously the elastic deformation progresses continuously, Young's modulus apparently decreases at the stress above the proportional limit. Therefore, the elastic deformation behavior, which does not obey Hooke's law, is observed. Similar to the case of the $TNTZ_{35}$ alloy, the amount of the strain of the specimen at the instant ε_l reaches ε_{emax} in the crystal direction where ε_{emax} is the smallest is considered to be equivalent to that at the proportional limit shown in Fig. 14.

The maximum recovery strain (in general recovery elastic strain + recovery strain due to the reverse transformation of the deformation-induced α″ martensite phase) of the $TNTZ_{30}$ alloy has been reported to increase with the strain of the specimen [10]. Therefore, this phenomenon of the increasing recovery strain cannot be explained by the mechanism mentioned above. Further investigations on the deformation mechanism of the $TNTZ_{30}$ alloy including the fully-plastically deformed region and texture analysis are needed.

4. Conclusions

Ti–XNb–10Ta–5Zr alloys were fabricated through powder metallurgy, forging and swaging processes based on the Ti–30Nb–10Ta–5Zr alloy, which was the composition that simplified that of the Ti–29Nb–13Ta–4.6Zr alloy for biomedical applications. The tensile deformation mechanisms of the Ti–25Nb–10Ta–5Zr, Ti–30Nb–10Ta–5Zr, and Ti–35Nb–

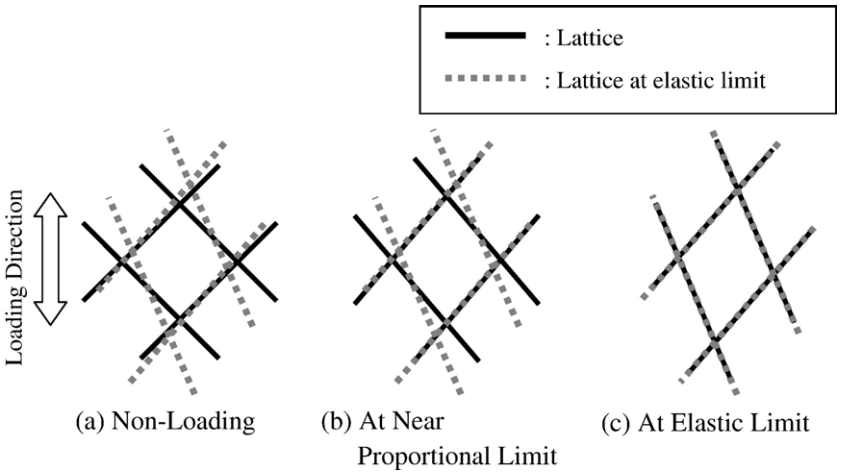

Fig. 17. Schematic drawing of deformation behavior of lattice in $TNTZ_{30}$ alloy.

10Ta–5Zr alloys were investigated using *in situ* X-ray diffraction analysis under several tensile loading conditions. The following results were obtained.

(1) Under the loading conditions, the X-ray diffraction peaks of the Ti–25Nb–10Ta–5Zr, Ti–30Nb–10Ta–5Zr, and Ti–35Nb–10Ta–5Zr alloys and Ti–15 V–3Cr–3Sn–3Al, A1070, and S45C alloys shift to higher angles than those obtained under the no–loading conditions in this study.

(2) The amount of the maximum elastic strain is remarkably different according the crystal orientation of the Ti-25Nb–10Ta–5Zr, Ti–30Nb–10Ta–5Zr, and Ti–35Nb–10Ta–5Zr alloys.

(3) For the Ti–30Nb–10Ta–5Zr alloy, the elastic deformation was considered to progress continuously in a different crystal direction although after the elastic strain reaches the elastic limit in the crystal direction where the elastic limit is the smallest, slip deformation occurred in that crystal direction. Therefore, the elastic modulus of this alloy appears to decrease in terms of strain over the proportional limit. Thus, the elastic deformation behavior of the Ti–30Nb–10Ta–5Zr alloy does not obey Hooke's law.

References

[1] D. Kuroda, M. Niinomi, K. Fukui, A. Suzuki, J. Hasegawa, Tetsu-to-Hagané 86 (2000) 610.
[2] T. Akahori, M. Niinomi, T. Maekawa, K. Fukui, A. Suzuki, J. Jpn. Inst. Met. 66 (2002) 715.
[3] M. Niinomi, T. Akahori, T. Yabunaka, K. Fukui, A. Suzuki, Tetsu-to-Hagané 88 (2002) 553.
[4] M. Niinomi, T. Akahori, S. Nakamura, K. Fukui, A. Suzuki, Tetsu-to-Hagané 88 (2002) 567.
[5] M. Niinomi, T. Akahori, K. Morikawa, T. Kasuga, A. Suzuki, H. Fukui, S. Niwa, Mater. Trans. 43 (2002) 2970.
[6] M. Niinomi, Biomaterials 24 (2003) 2673.
[7] E.B. Taddei, V.A.R. Henriques, C.R.M. Silva, C.A.A. Cairo, Mater. Sci. Eng., C, Biomim. Mater., Sens. Syst. 24 (2004) 683.
[8] N. Sakaguchi, M. Niinomi, T. Akahori, T. Saito, T. Furuta, J. Jpn. Inst. Met. 67 (2003) 681.
[9] N. Sakaguchi, M. Niinomi, T. Akahori, T. Saito, T. Furuta, J. Jpn. Inst. Met. 68 (2004) 1076.
[10] N. Sakaguchi, M. Niinomi, T. Akahori, Mater. Trans. 45 (2004) 1113.
[11] N. Sakaguchi, M. Niinomi, T. Akahori, Mater. Sci. Eng., C, Biomim. Mater., Sens. Syst. 25 (2005) 363.
[12] N. Sakaguchi, M. Niinomi, T. Akahori, Mater. Sci. Eng., C, Biomim. Mater., Sens. Syst. 25 (2005) 370.
[13] L.F. Mondolfo, Aluminum Alloys, Structure and Properties, Butterworths, 1976, p. 72.
[14] C.R. Krenn, D. Roundy, J.W. Morris Jr., M.L. Cohen, Mater. Sci. Eng., A Struct. Mater.: Prop. Microstruct. Process. 319321 (2001) 111.
[15] T. Grosdidier, M.J. Philippe, Mater. Sci. Eng., A Struct. Mater.: Prop. Microstruct. Process. 291 (2000) 218.
[16] Y. Ohmori, T. Ogo, K. Nakai, S. Kobayashi, Mater. Sci. Eng., A Struct. Mater.: Prop. Microstruct. Process. 321 (2001) 182.